

Entanglement Detection with Variational Quantum Interference: Theory and Experiment

Rui Zhang,^{1,2,*} Zhenhuan Liu,^{3,*} Chendi Yang,³ Yue-Yang Fei,^{1,2,4} Xu-Fei Yin,^{1,2,4}
Yingqiu Mao,^{1,2,4} Li Li,^{1,2,4} Nai-Le Liu,^{1,2,4} Yu-Ao Chen,^{1,2,4,5} and Jian-Wei Pan^{1,2,4}

¹*Hefei National Research Center for Physical Sciences at the Microscale and School of Physical Sciences,
University of Science and Technology of China, Hefei 230026, China*

²*Shanghai Research Center for Quantum Science and CAS Center
for Excellence in Quantum Information and Quantum Physics,
University of Science and Technology of China, Shanghai 201315, China*

³*Center for Quantum Information, Institute for Interdisciplinary
Information Sciences, Tsinghua University, Beijing 100084, China*

⁴*Hefei National Laboratory, University of Science and Technology of China, Hefei 230088, China*

⁵*New Cornerstone Science Laboratory, School of Emergent Technology,
University of Science and Technology of China, Hefei 230026, China*

Entanglement detection serves as a fundamental task in quantum information science, playing a critical role in quantum benchmarking and foundational studies. As the number of controllable qubits continues to increase, there emerges a pressing demand for scalable and robust entanglement detection protocols that can maintain high detection capability while requiring minimal resources. By integrating the positive partial transposition criterion with variational quantum interference, we develop an entanglement detection protocol that requires moderate classical and quantum computation resources. Numerical simulations demonstrate that this protocol attains high detection capability using only shallow quantum circuits, outperforming several widely-used entanglement detection methods. The protocol also exhibits strong resilience to circuit noise, ensuring its applicability across different physical platforms. Experimental implementation on a linear optical platform successfully identifies entanglement in a three-qubit mixed state that cannot be detected by conventional entanglement witnesses. Drawing upon the full potential of quantum and classical resources, our protocol paves a new path for efficient entanglement detection.

Introduction. Quantum entanglement, one of the distinguishing features of quantum physics [1], provides advantages to a variety of quantum information tasks, including quantum computation [2, 3], quantum cryptography [4, 5], and quantum metrology [6, 7], as well as offers new perspectives for quantum many-body physics [8–10]. Therefore, the ability to generate large-scale entanglement has been widely utilized to showcase the superior capabilities of quantum devices [11–22]. With the rapid development of quantum technologies, we have reached a stage that the manipulation of hundreds of qubits is achievable [23–25]. Therefore, finding scalable, effective, and robust entanglement detection schemes constitutes a key objective in quantum information research.

In a typical entanglement detection experiment, researchers first prepare a target state and then experimentally verify its entanglement. When the experimentally prepared state approximates the target state with sufficient fidelity, protocols including entanglement witnesses (EWs) [11–14, 17–19, 21] and Bell tests [26–30] can be specially tailored to efficiently and effectively verify the entanglement. However, the performance of these protocols is highly susceptible to unpredictable noise, leading to a rapid loss of detection capability under practical experimental conditions [31, 32]. To address these limitations while eliminating dependence on a priori knowl-

edge of the target state, researchers adopted the positive partial transposition (PPT) criterion [33], which exhibits reliable performance even for highly mixed states [34, 35]. Nevertheless, the implementation of PPT criterion typically requires either complex joint operations [36] or classical post-processing of measurement data that scales exponentially with system size [37–39]. Alternative approaches incorporating variational quantum algorithms for parameter optimization—including machine learning-based methods [40–42] and adversarial solvers [43]—have emerged as promising directions. However, these methods demand either extensive computational resources for training data or the implementation of deep variational quantum circuits.

In this work, leveraging the detection capability of the PPT criterion and flexibility of variational quantum algorithms, we propose the *interferometric PPT* (iPPT) protocol, as illustrated in Fig. 1. The iPPT protocol demonstrates advantages in both classical and quantum resource efficiency. First, it avoids processing exponentially large classical datasets by eliminating the need for reference state information. Second, inheriting the strong detection capability of PPT criterion, we numerically show that iPPT protocol exhibits superior detection capability compared to conventional methods such as fidelity [44, 45] and purity criteria [16, 20] with shallow reference state preparation circuits. Notably, when a single layer of Bell state measurements (BSMs) is experimentally accessible, the iPPT protocol exhibits inherent

* These authors contributed equally to this work.

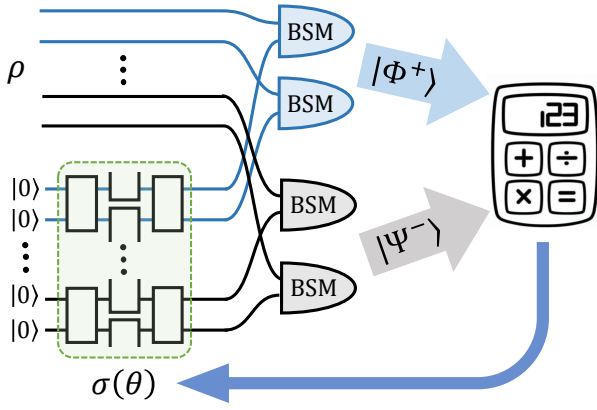


FIG. 1. Overview of iPPT protocol. For a target state ρ , the initial step involves preparing a reference state $\sigma(\theta)$ using the variational circuit (light green box). Subsequently, Bell state measurements (BSMs) are carried out on each corresponding qubit pair from the target state ρ and the reference state $\sigma(\theta)$. Lines in blue and black represent qubits of subsystems A and B of target and reference states. BSM modules in blue and black collect data associated with the Bell states $|\Phi^+\rangle = (|00\rangle + |11\rangle)/\sqrt{2}$ and $|\Psi^-\rangle = (|01\rangle - |10\rangle)/\sqrt{2}$, respectively. The collected data are post-processed to determine the entanglement property of the target state ρ , with a negative result of $\text{Tr}(\rho\sigma^{\text{T}A})$ indicating the existence of entanglement.

robustness to noise in the reference state preparation circuit, a property derived from the PPT criterion. We experimentally implement the iPPT protocol to conduct a proof-of-principle entanglement detection on a three-qubit mixed state in a linear optical platform. The experimental results highlight the effectiveness of our protocol in detecting entanglement in mixed states that conventional entanglement witness protocols fail to identify.

Protocol. The PPT criterion is widely used in entanglement studies for its concise mathematical form and powerful detection capability [34, 35, 46]. The criterion operates by assessing the semi-positivity of $\rho^{\text{T}A}$ with T_A being the partial transposition operation on a subsystem A , where the negative eigenvalues of $\rho^{\text{T}A}$ indicate the entanglement. Since the partial transposition is not directly implementable in physical systems, it is imperative to devise feasible entanglement detection protocols that harness the detection power of PPT criterion while conserving resources. Our protocol is inspired by the EW-based PPT protocol [47], which shows that verifying PPT criterion is equivalent to finding a reference state $|\psi(\theta)\rangle$ satisfying

$$\langle\psi(\theta)|\rho^{\text{T}A}|\psi(\theta)\rangle = \text{Tr}[\rho\sigma(\theta)^{\text{T}A}] < 0, \quad (1)$$

where $\sigma(\theta) = |\psi(\theta)\rangle\langle\psi(\theta)|$. In principle, one can search over many different observables $\sigma(\theta)^{\text{T}A}$, which are actually EWs, to find a negative expectation value. However, even if restricting $|\psi(\theta)\rangle$ to be a shallow circuit state, this protocol still requires significant classical and quantum resources. Firstly, one needs to classically store and process $\sigma(\theta)^{\text{T}A}$, an exponentially large matrix, to know

how to experimentally measure this observable. Besides, the measurement of $\sigma(\theta)^{\text{T}A}$ requires to rotate ρ to the eigen-basis of $\sigma(\theta)^{\text{T}A}$. Although $|\psi(\theta)\rangle$ is a shallow circuit state, the rotation unitary might require a much deeper quantum circuit to implement, as there exists no clear relationship between circuits preparing $|\psi(\theta)\rangle$ and diagonalizing $\sigma(\theta)^{\text{T}A}$.

To ease the difficulties, we propose the iPPT protocol, which is based on the following observation [48]:

Observation 1. Given two bipartite quantum state ρ and σ , it satisfies

$$\text{Tr}(\rho\sigma^{\text{T}A}) = \text{Tr}[(\rho \otimes \sigma)(\Phi_A^+ \otimes S_B)], \quad (2)$$

where A and B are two complementary subsystems of ρ with n_A and n_B qubits, $\Phi_A^+ = \sum_{i,j=0}^{2^{n_A}-1} |ii\rangle\langle jj|$ stands for the unnormalized maximally entangled state defined on subsystem A , and $S_B = \sum_{i,j=0}^{2^{n_B}-1} |ij\rangle\langle ji|$ is the SWAP operator defined on subsystem B .

When considering multi-qubit scenarios, Φ^+ and S all have tensor product structures, i.e., $\Phi^+ = \bigotimes_i \Phi_i^+$ and $S = \bigotimes_i S_i$. Here, Φ_i^+ is the unnormalized Bell state $(|00\rangle + |11\rangle)(\langle 00| + \langle 11|)$ and the two-qubit SWAP operator can be written as $S_i = (\mathbb{I} - \Psi^-)$, where \mathbb{I} is the identity operator and $\Psi^- = (|01\rangle - |10\rangle)(\langle 01| - \langle 10|)$ is another unnormalized Bell state. Based on this observation, we can estimate the value of $\text{Tr}(\rho\sigma^{\text{T}A})$ using BSMs performed between ρ and σ , as shown by the circuit in Fig. 1. Specifically, labeling the measurement outcome of each BSM as $r_{i,j} \in \{0, 1, 2, 3\}$, which corresponds to the four Bell states $\{|\Phi^+\rangle, |\Phi^-\rangle, |\Psi^+\rangle, |\Psi^-\rangle\}$, the unbiased estimator for $\text{Tr}(\rho\sigma^{\text{T}A})$ is

$$\text{Tr}(\rho\sigma^{\text{T}A}) = \prod_{i=0}^{(n_A-1)} \prod_{j=n_A}^{(n_A+n_B-1)} 2\delta_{r_i,0}(1 - 2\delta_{r_j,3}). \quad (3)$$

Therefore, the quantum experiment of iPPT protocol consists two stages, as illustrated in Fig. 1. The first stage involves preparing the reference state $\sigma(\theta)$ with a parameterized quantum circuit. The second stage is the measurement of observable $\Phi_A^+ \otimes S_B$ using BSMs. In contrast to the classical information utilized in the EW-based PPT protocol, the iPPT protocol enables physical preparation of the parameterized reference state $\sigma(\theta)$, with the partial transposition operation being encapsulated into the observable. Consequently, classical computers in iPPT protocol are primarily utilized for processing BSM outcomes and adjusting parameters, significantly mitigating the classical cost of the EW-based PPT protocol. Besides, the measurement procedure in iPPT only requires a single layer of two-qubit gates, making it applicable to diverse physical platforms, such as linear optics [14] and cold atoms [15, 16]. Moreover, the iPPT protocol exhibits inherent robustness against errors occurring in the reference state preparation circuit which may be much deeper than the BSM circuit. The reason

is that, $\sigma(\theta)^{T_A}$, with $\sigma(\theta)$ being a mixed state, remains a valid entanglement witness. Thus, as long as BSM can be effectively executed, negative measurement values can faithfully reflect the existence of entanglement in the target state ρ .

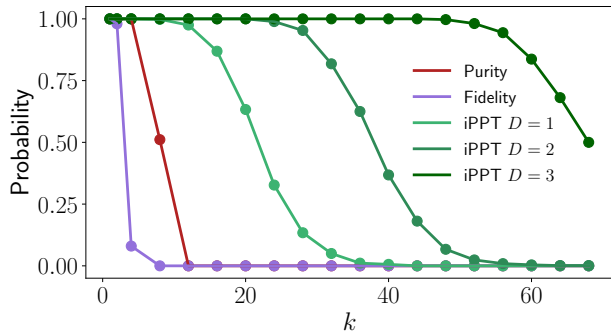


FIG. 2. Entanglement detection capability of the iPPT protocol with various depth of the reference state preparation circuits, D , in comparison with the purity and fidelity criteria. For each point, we randomly sample 1000 six-qubit mixed states and verify their entanglement using different entanglement detection criteria. The y -coordinate stands for the success probability for verifying the entanglement of the sampled six-qubit mixed state. The larger values of x -coordinate term, k , correspond to the lower expected purity of the sampled mixed states.

Numerical simulation. Inheriting the entanglement detection power of PPT criterion, we will show that iPPT protocol performs well even with shallow reference state preparation circuits. Through numerical simulations, we assess the detection capability of iPPT protocol under various reference state preparation circuit depths D , comparing it against purity [49] and fidelity-based [50] entanglement detection criteria. The reason behind selecting these two protocols is that both purity and fidelity can be measured using BSMs. Thus, these two protocols do not require extra classical and quantum resources as iPPT protocol and have been experimentally implemented in various physical platforms [11–22]. To assess the entanglement detection capabilities of these protocols against random mixed states, we apply them to a set of six-qubit mixed states sampled with the following procedure: We generate a large number of $(2^6 \times k)$ -dimensional random pure states and subsequently trace out the k -dimensional subsystem to create six-qubit mixed states. The parameter k actually quantifies the degree of mixedness of these states. A larger value of k indicates a less purity and less entanglement of the generated six-qubit mixed states. As illustrated in Fig. 2, the iPPT protocol exhibits significantly superior performance relative to purity and fidelity protocols, even when employing very shallow circuits, and maintains a high detection capability even for highly mixed states. The details of numerical experiments are left in Appendix B.

Experimental demonstration. After numerically demonstrating the detection capability, we devise a

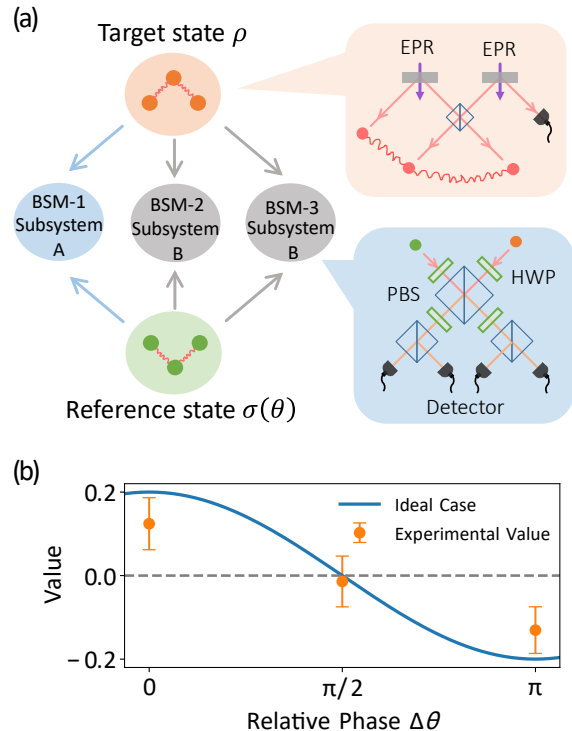


FIG. 3. Experimental design and results. (a) The three-qubit target state ρ and reference state $\sigma(\theta)$ are prepared with two pairs of entangled photons, respectively. Three BSMs are performed between three pairs of photons from the reference and target state. Based on the measured results, the value of $\text{Tr}(\rho\sigma^{T_A})$ can be estimated. (b) Ideal and experimental value of $\text{Tr}(\rho\sigma^{T_A})$ with respect to the variable phase parameter $\Delta\theta$.

proof-of-principle experiment in linear optical platform to show the practicality of iPPT protocol. We consider the three-qubit bipartite state

$$\rho = 0.5\rho_1 + 0.5\rho_2, \quad (4)$$

where ρ_1 and ρ_2 are Greenberger–Horne–Zeilingler (GHZ) states with phase-flipping error,

$$\begin{aligned} \rho_1 &= F_1^+ (|000\rangle + |111\rangle)(\langle 000| + \langle 111|) \\ &\quad + F_1^- (|000\rangle - |111\rangle)(\langle 000| - \langle 111|), \\ \rho_2 &= F_2^+ (|100\rangle + |011\rangle)(\langle 100| + \langle 011|) \\ &\quad + F_2^- (|100\rangle - |011\rangle)(\langle 100| - \langle 011|). \end{aligned} \quad (5)$$

By setting four coefficients to be $F_1^+ = F_2^+ = 0.9$ and $F_1^- = F_2^- = 0.1$, the proportions of all four main component states of ρ are less than 0.5. We show in Appendix C that its entanglement cannot be identified with conventional fidelity-based entanglement witness protocols [47]. With the prior knowledge of the target state ρ , we can customize the parameterized reference state $\sigma(\Delta\theta) = |\psi(\Delta\theta)\rangle\langle\psi(\Delta\theta)|$ with

$$|\psi(\Delta\theta)\rangle = \frac{1}{\sqrt{2}}(|010\rangle + e^{i\Delta\theta}|101\rangle), \quad (6)$$

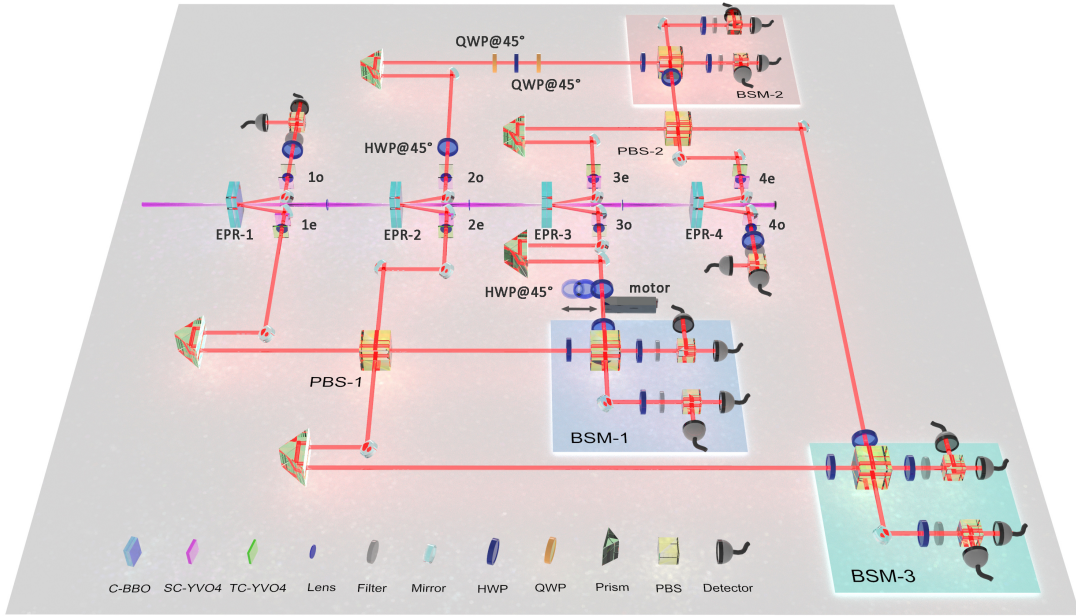


FIG. 4. Schematic of experimental setup for iPPT protocol. The pulsed ultraviolet pump laser successively passes through four separated C-BBO crystals from left to right and generate four EPR entangled photon pairs, $|\text{EPR}\rangle = (|HH\rangle + |VV\rangle)/\sqrt{2}$. The first two EPR sources, EPR-1 and EPR-2, are used to prepare the reference state. The last two EPR sources, EPR-3 and EPR-4, are used to prepare the to-be-verified target state. The mixing of each component state of the target state is achieved by a one-dimensional linear motor (“motor” in schematic) that randomly introducing the polarization flipping. The three pairs of photons from reference state and target state are introduced to three BSM device, which are composed of PBSs, HWPs, and single-photon detectors. SC-YVO4 and TC-YVO4 are YVO₄ crystals used for spatial compensation (SC) and temporal compensation (TC) of each EPR source.

to evaluate its entanglement, where $\Delta\theta$ is the variable phase parameter. In this case, as shown in Fig. 3(a), by assigning the first qubit as the subsystem A and the other two qubits as the subsystem B , the value of $\text{Tr}[\rho\sigma(\Delta\theta)^{T_A}]$ with respect to the phase parameter $\Delta\theta$ can be calculated as the blue solid curve in Fig. 3(b). When $\Delta\theta$ is in the interval $(\pi/2, \pi)$, the value of $\text{Tr}[\rho\sigma(\Delta\theta)^{T_A}]$ is negative, and the entanglement in the mixed target state ρ can be clearly identified.

We perform the experimental demonstration of iPPT entanglement detection protocol in an eight-photon entanglement platform as depicted in Fig. 4. In our experiment, a beam of pulsed laser with the central wavelength of 390 nm is successively focused on four sandwich-like β -barium borate crystal combinations (C-BBO). With the type-II spontaneous parametric down-conversion (SPDC) process, each of the four C-BBO can generate a pair of Einstein–Podolsky–Rosen (EPR) entangled photons, $|\text{EPR}\rangle = (|HH\rangle + |VV\rangle)/\sqrt{2}$. The states $|H\rangle$ and $|V\rangle$ represent the horizontal and vertical polarization state of photons, which encode states $|0\rangle$ and $|1\rangle$, respectively. The first two EPR sources (EPR-1 and EPR-2) are used to prepare the parameterized reference state $\sigma(\Delta\theta)$, with photons 1e-2o-2e. The last two EPR sources (EPR-3 and EPR-4) are used to prepare the target state ρ in the form of Eq. (4), with photons 3e-3o-4e. Coefficients of each component state in Eq. (5) are mainly determined by the two-photon interference visibility on

the polarizing beam splitter (PBS), with details left in Appendix D. After the state preparation, corresponding photons of reference and target state are introduced into three PBSs to perform three BSMs. The BSM module, consisting of half-wavelength plates (HWPs), PBSs, and single-photon detectors, can distinguish any two from the four Bell states in a single trial [51].

In the experiment, the pump laser power is set to be 400 mW, and band-pass filters with the full width at half maximum of 4 nm are applied to down-converted photons. As a result, the target state is prepared with fidelity to be 0.977 with respect to the ideal one in Eq. (4). The proportions of the four main component states are measured to be $\frac{F_1^+}{2} = 0.418$, $\frac{F_1^-}{2} = 0.060$, $\frac{F_2^+}{2} = 0.448$, and $\frac{F_2^-}{2} = 0.035$. Since all of these coefficient are less than 0.5, entanglement of the prepared target state cannot be detected using common fidelity-based EW methods [47]. As for the three BSM devices, the visibility of the Hong-Ou-Mandel-type two-photon interference at each of the three PBSs is measured to be 81.9%, 83.6%, and 84.9%.

In the experiment, we use iPPT protocol to verify entanglement of the prepared target state. We estimate the value of $\text{Tr}[\rho\sigma(\Delta\theta)^{T_A}]$ with three different $\Delta\theta$ and plot corresponding experimental values as orange dots in Fig. 3(b). The trend of $\text{Tr}[\rho\sigma(\Delta\theta)^{T_A}]$ with respect to various relative phases $\Delta\theta$ is consistent with the theo-

retical curve. Deviation of the experimental results from the theoretical curve is mainly due to the imperfection of the BSs. The negative experimental result for the reference state with $\Delta\theta = \pi$ unequivocally identifies the entanglement of the prepared target state ρ_{exp} .

Discussion. Entanglement detection is widely recognized to be a challenging task [31]. Although the iPPT protocol does not address all the challenges associated with entanglement detection, it introduces valuable methods to enhance classical computational resources, robustness, and scalability. Besides, the iPPT protocol provides a mean to trade between the detection capability and quantum resources. As shown in Fig. 2, the detection power of iPPT protocol increases with the depth of the reference state preparation circuit. However, due to the trade-off between the expressibility and trainability of variational quantum algorithms [52–54], the increment of circuit depth would bring difficulties to the parameter training. Thus, in practical scenarios, it is crucial to utilize the prior knowledge of the target state ρ to design more efficient ansatz, just like Eq. (6).

In addition to the PPT criterion, Observation 1 can be generalized to a general positive map criterion as

$$\text{Tr}[\mathcal{N}_A \otimes \mathcal{I}_B(\rho)\psi] = \text{Tr}[(\rho \otimes \psi)(W_A \otimes S_B)], \quad (7)$$

where W is an entanglement witness and \mathcal{N} is a positive

map determined by W . As the positive map criterion normally has exponentially higher detection capability compared with the entanglement witness [31], Eq. (7) provides us a systematic way to enhance the detection capability of an entanglement witness utilizing the same logic as iPPT.

Acknowledgement. We appreciate the helpful discussions with Xiongfeng Ma, Otfried Gühne, Satoya Imai, Andreas Elben, Daniel Miller, You Zhou, Hong-Ye Hu, and Zhenyu Cai. This work was supported by the National Natural Science Foundation of China (Grants No. 11975222, No. 11874340, No. 12174216), Shanghai Municipal Science and Technology Major Project (Grant No. 2019SHZDZX01), Chinese Academy of Sciences and the Shanghai Science and Technology Development Funds (Grant No. 18JC1414700), the Innovation Program for Quantum Science and Technology (Grant No. 2021ZD0301901, No. 2021ZD0300804), the Basic Science Center Project of NSFC (Grant No. 12488301), and the New Cornerstone Science Foundation. Xu-Fei Yin was support from the China Postdoctoral Science Foundation (Grant No. 2023M733418). The numerical simulations are mainly performed by using MindSpore Quantum [55] with updated code available at [Gitee](https://gitee.com/mindsore).

-
- [1] R. Horodecki, P. Horodecki, M. Horodecki, and K. Horodecki, Quantum entanglement, *Rev. Mod. Phys.* **81**, 865 (2009).
- [2] M. A. Nielsen and I. L. Chuang, *Quantum Computation and Quantum Information: 10th Anniversary Edition* (Cambridge University Press, 2010).
- [3] R. Jozsa and N. Linden, On the role of entanglement in quantum-computational speed-up, *Proceedings of the Royal Society A* **459**, 2011 (2003).
- [4] N. Gisin, G. Ribordy, W. Tittel, and H. Zbinden, Quantum cryptography, *Rev. Mod. Phys.* **74**, 145 (2002).
- [5] A. K. Ekert, Quantum cryptography based on Bell’s theorem, *Phys. Rev. Lett.* **67**, 661 (1991).
- [6] V. Giovannetti, S. Lloyd, and L. Maccone, Quantum-enhanced measurements: beating the standard quantum limit, *Science* **306**, 1330 (2004).
- [7] V. Giovannetti, S. Lloyd, and L. Maccone, Advances in quantum metrology, *Nature Photonics* **5**, 222 (2011).
- [8] L. Amico, R. Fazio, A. Osterloh, and V. Vedral, Entanglement in many-body systems, *Rev. Mod. Phys.* **80**, 517 (2008).
- [9] N. Lafflorencie, Quantum entanglement in condensed matter systems, *Physics Reports* **646**, 1 (2016).
- [10] D. A. Abanin, E. Altman, I. Bloch, and M. Serbyn, Colloquium: Many-body localization, thermalization, and entanglement, *Rev. Mod. Phys.* **91**, 021001 (2019).
- [11] H. Häffner, W. Hänsel, C. F. Roos, J. Benhelm, D. Chekhal kar, M. Chwalla, T. Körber, U. D. Rapol, M. Riebe, P. O. Schmidt, C. Becher, O. Gühne, W. Dür, and R. Blatt, Scalable multiparticle entanglement of trapped ions, *Nature* **438**, 643 (2005).
- [12] D. Leibfried, E. Knill, S. Seidelin, J. Britton, R. B. Blakestad, J. Chiaverini, D. B. Hume, W. M. Itano, J. D. Jost, C. Langer, R. Ozeri, R. Reichle, and D. J. Wineland, Creation of a six-atom ‘Schrödinger cat’ state, *Nature* **438**, 639 (2005).
- [13] T. Monz, P. Schindler, J. T. Barreiro, M. Chwalla, D. Nigg, W. A. Coish, M. Harlander, W. Hänsel, M. Hennrich, and R. Blatt, 14-qubit entanglement: Creation and coherence, *Phys. Rev. Lett.* **106**, 130506 (2011).
- [14] J.-W. Pan, Z.-B. Chen, C.-Y. Lu, H. Weinfurter, A. Zeilinger, and M. Żukowski, Multiphoton entanglement and interferometry, *Rev. Mod. Phys.* **84**, 777 (2012).
- [15] R. Islam, R. Ma, P. M. Preiss, M. Eric Tai, A. Lukin, M. Rispoli, and M. Greiner, Measuring entanglement entropy in a quantum many-body system, *Nature* **528**, 77 (2015).
- [16] A. M. Kaufman, M. E. Tai, A. Lukin, M. Rispoli, R. Schittko, P. M. Preiss, and M. Greiner, Quantum thermalization through entanglement in an isolated many-body system, *Science* **353**, 794 (2016).
- [17] X.-L. Wang, Y.-H. Luo, H.-L. Huang, M.-C. Chen, Z.-E. Su, C. Liu, C. Chen, W. Li, Y.-Q. Fang, X. Jiang, J. Zhang, L. Li, N.-L. Liu, C.-Y. Lu, and J.-W. Pan, 18-qubit entanglement with six photons’ three degrees of freedom, *Phys. Rev. Lett.* **120**, 260502 (2018).
- [18] A. Omran, H. Levine, A. Keesling, G. Semeghini, T. T. Wang, S. Ebadi, H. Bernien, A. S. Zibrov, H. Pichler, S. Choi, J. Cui, M. Rossignolo, P. Rembold, S. Mon-

- tangero, T. Calarco, M. Endres, M. Greiner, V. Vuletić, and M. D. Lukin, Generation and manipulation of schrödinger cat states in rydberg atom arrays, *Science* **365**, 570 (2019).
- [19] C. Song, K. Xu, H. Li, Y.-R. Zhang, X. Zhang, W. Liu, Q. Guo, Z. Wang, W. Ren, J. Hao, H. Feng, H. Fan, D. Zheng, D.-W. Wang, H. Wang, and S.-Y. Zhu, Generation of multicomponent atomic Schrödinger cat states of up to 20 qubits, *Science* **365**, 574 (2019).
- [20] T. Brydges, A. Elben, P. Jurcevic, B. Vermersch, C. Maier, B. P. Lanyon, P. Zoller, R. Blatt, and C. F. Roos, Probing Rényi entanglement entropy via randomized measurements, *Science* **364**, 260 (2019).
- [21] S. Cao, B. Wu, F. Chen, M. Gong, Y. Wu, Y. Ye, C. Zha, H. Qian, C. Ying, S. Guo, Q. Zhu, H.-L. Huang, Y. Zhao, S. Li, S. Wang, J. Yu, D. Fan, D. Wu, H. Su, H. Deng, H. Rong, Y. Li, K. Zhang, T.-H. Chung, F. Liang, J. Lin, Y. Xu, L. Sun, C. Guo, N. Li, Y.-H. Huo, C.-Z. Peng, C.-Y. Lu, X. Yuan, X. Zhu, and J.-W. Pan, Generation of genuine entanglement up to 51 superconducting qubits, *Nature* **619**, 738 (2023).
- [22] A. L. Shaw, Z. Chen, J. Choi, D. K. Mark, P. Scholl, R. Finkelstein, A. Elben, S. Choi, and M. Endres, Benchmarking highly entangled states on a 60-atom analog quantum simulator, [arXiv:2308.07914](https://arxiv.org/abs/2308.07914) (2023).
- [23] Y. Kim, A. Eddins, S. Anand, K. X. Wei, E. van den Berg, S. Rosenblatt, H. Nayfeh, Y. Wu, M. Zaletel, K. Temme, and A. Kandala, Evidence for the utility of quantum computing before fault tolerance, *Nature* **618**, 500 (2023).
- [24] D. Bluvstein, S. J. Evered, A. A. Geim, S. H. Li, H. Zhou, T. Manovitz, S. Ebadi, M. Cain, M. Kalinowski, D. Hangleiter, J. P. Bonilla Ataides, N. Maskara, I. Cong, X. Gao, P. Sales Rodriguez, T. Karolyshyn, G. Semeghini, M. J. Gullans, M. Greiner, V. Vuletić, and M. D. Lukin, Logical quantum processor based on reconfigurable atom arrays, *Nature* **626**, 58 (2024).
- [25] T. Jiang, J. Cai, J. Huang, N. Zhou, Y. Zhang, J. Bei, G. Cai, S. Cao, F. Chen, J. Chen, *et al.*, Generation of 95-qubit genuine entanglement and verification of symmetry-protected topological phases, [arXiv:2505.01978](https://arxiv.org/abs/2505.01978) (2025).
- [26] J.-W. Pan, D. Bouwmeester, M. Daniell, H. Weinfurter, and A. Zeilinger, Experimental test of quantum nonlocality in three-photon Greenberger-Horne-Zeilinger entanglement, *Nature* **403**, 515 (2000).
- [27] P. Hyllus, O. Gühne, D. Bruß, and M. Lewenstein, Relations between entanglement witnesses and Bell inequalities, *Phys. Rev. A* **72**, 012321 (2005).
- [28] T. Moroder, J.-D. Bancal, Y.-C. Liang, M. Hofmann, and O. Gühne, Device-independent entanglement quantification and related applications, *Phys. Rev. Lett.* **111**, 030501 (2013).
- [29] R. Arnon-Friedman and J.-D. Bancal, Device-independent certification of one-shot distillable entanglement, *New Journal of Physics* **21**, 033010 (2019).
- [30] Y. Zhu, X. Zhang, and X. Ma, Entanglement quantification via nonlocality, [arXiv:2303.08407](https://arxiv.org/abs/2303.08407) (2023).
- [31] P. Liu, Z. Liu, S. Chen, and X. Ma, Fundamental limitation on the detectability of entanglement, *Phys. Rev. Lett.* **129**, 230503 (2022).
- [32] D. Miller, D. Loss, I. Tavernelli, H. Kampermann, D. Bruß, and N. Wyderka, Shor-Laflamme distributions of graph states and noise robustness of entanglement, *Journal of Physics A: Mathematical and Theoretical* **56**, 335303 (2023).
- [33] A. Peres, Separability criterion for density matrices, *Phys. Rev. Lett.* **77**, 1413 (1996).
- [34] G. AUBRUN, Partial transposition of random states and non-centered semicircular distributions, *Random Matrices: Theory and Applications* **01**, 1250001 (2012).
- [35] B. Collins and I. Nechita, Random matrix techniques in quantum information theory, *Journal of Mathematical Physics* **57**, 015215 (2016).
- [36] H. A. Carteret, Noiseless quantum circuits for the Peres separability criterion, *Phys. Rev. Lett.* **94**, 040502 (2005).
- [37] A. Elben, R. Kueng, H.-Y. R. Huang, R. van Bijnen, C. Kokail, M. Dalmonte, P. Calabrese, B. Kraus, J. Preskill, P. Zoller, and B. Vermersch, Mixed-state entanglement from local randomized measurements, *Phys. Rev. Lett.* **125**, 200501 (2020).
- [38] Y. Zhou, P. Zeng, and Z. Liu, Single-copies estimation of entanglement negativity, *Phys. Rev. Lett.* **125**, 200502 (2020).
- [39] K. Wang, Z. Song, X. Zhao, Z. Wang, and X. Wang, Detecting and quantifying entanglement on near-term quantum devices, *npj Quantum Information* **8**, 52 (2022).
- [40] J. Gray, L. Banchi, A. Bayat, and S. Bose, Machine-learning-assisted many-body entanglement measurement, *Phys. Rev. Lett.* **121**, 150503 (2018).
- [41] S. Lu, S. Huang, K. Li, J. Li, J. Chen, D. Lu, Z. Ji, Y. Shen, D. Zhou, and B. Zeng, Separability-entanglement classifier via machine learning, *Phys. Rev. A* **98**, 012315 (2018).
- [42] J. Roik, K. Bartkiewicz, A. Černoč, and K. Lemr, Accuracy of entanglement detection via artificial neural networks and human-designed entanglement witnesses, *Phys. Rev. Appl.* **15**, 054006 (2021).
- [43] X.-F. Yin, Y. Du, Y.-Y. Fei, R. Zhang, L.-Z. Liu, Y. Mao, T. Liu, M.-H. Hsieh, L. Li, N.-L. Liu, D. Tao, Y.-A. Chen, and J.-W. Pan, Efficient bipartite entanglement detection scheme with a quantum adversarial solver, *Phys. Rev. Lett.* **128**, 110501 (2022).
- [44] M. Weilenmann, B. Dive, D. Trillo, E. A. Aguilar, and M. Navascués, Entanglement detection beyond measuring fidelities, *Phys. Rev. Lett.* **124**, 200502 (2020).
- [45] O. Gühne, Y. Mao, and X.-D. Yu, Geometry of faithful entanglement, *Phys. Rev. Lett.* **126**, 140503 (2021).
- [46] G. Vidal and R. F. Werner, Computable measure of entanglement, *Phys. Rev. A* **65**, 032314 (2002).
- [47] O. Gühne and G. Tóth, Entanglement detection, *Physics Reports* **474**, 1 (2009).
- [48] A. Rico and F. Huber, Entanglement detection with trace polynomials, *Phys. Rev. Lett.* **132**, 070202 (2024).
- [49] The purity criterion states that when $\text{Tr}(\rho_A^2) < \text{Tr}(\rho^2)$ with ρ_A being the reduced density matrix of ρ , then ρ is entangled.
- [50] The fidelity criterion states that when $\langle \psi | \rho | \psi \rangle > \alpha$ with α being the square of the maximal Schmidt value of $|\psi\rangle$, then ρ is entangled.
- [51] J.-W. Pan and A. Zeilinger, Greenberger-Horne-Zeilinger-state analyzer, *Phys. Rev. A* **57**, 2208 (1998).
- [52] J. R. McClean, S. Boixo, V. N. Smelyanskiy, R. Babush, and H. Neven, Barren plateaus in quantum neural network training landscapes, *Nature Communications* **9**, 4812 (2018).
- [53] Z. Holmes, K. Sharma, M. Cerezo, and P. J. Coles, Connecting ansatz expressibility to gradient magnitudes and

- barren plateaus, *PRX Quantum* **3**, 010313 (2022).
- [54] L.-W. Yu, W. Li, Q. Ye, Z. Lu, Z. Han, and D.-L. Deng, Expressibility-induced concentration of quantum neural tangent kernels, *arXiv:2311.04965* (2023).
- [55] M. Developer, *Mindquantum*, version 0.9.11 (2021).
- [56] M. Horodecki, P. Horodecki, and R. Horodecki, Separability of mixed states: necessary and sufficient conditions, *Physics Letters A* **223**, 1 (1996).

Appendix A: Theoretical Analysis

Using the Choi matrix representation, the action of a map can be represented as

$$\mathcal{N}(\rho) = \text{Tr} [\Lambda_{\mathcal{N}} (\rho^T \otimes \mathbb{I})] = \text{Tr} [\Lambda_{\mathcal{N}} \rho^T] = \text{Tr} [\Lambda_{\mathcal{N}} \rho], \quad (\text{A1})$$

where $\Lambda_{\mathcal{N}}$ is the Choi matrix of map \mathcal{N} , legs represent indices of matrices, and legs connection stands for the indices contraction. With this tool, the inner product can be represented as

$$\text{Tr} [\mathcal{N}_A \otimes \mathcal{I}_B(\rho)\psi] = \text{Tr} [\Lambda_{\mathcal{N}} \rho \psi] = \text{Tr} [\Lambda_{\mathcal{N}}^T \rho \psi], \quad (\text{A2})$$

where the grey dashed lines represent trace functions, blue and black legs represent indices of subsystem A and B , respectively. As is known, the Choi matrix of a positive map, together with its partial transposition, are valid entanglement witnesses [56]. Therefore, we can prove that

$$\text{Tr} [\mathcal{N}_A \otimes \mathcal{I}_B(\rho)\psi] = \text{Tr} [(\rho \otimes \psi) (W_A \otimes S_B)]. \quad (\text{A3})$$

Assuming \mathcal{N} to be the transposition map, we have the main result of this work, $\text{Tr} [\rho^{T_A} \psi] = \text{Tr} [(\rho \otimes \psi) (\Phi_A^+ \otimes S_B)]$.

Appendix B: Details of Numerical Experiments

In the main context, we discussed the fidelity-based entanglement witness protocol. Specifically, this protocol is based on the entanglement witness

$$W = \alpha \mathbb{I} - |\psi\rangle\langle\psi|, \quad (\text{B1})$$

where \mathbb{I} is the identity operator and α is the square of the maximal Schimdt number of $|\psi\rangle$. The verification of this protocol is equivalent with verifying if the fidelity between the target state ρ and $|\psi\rangle$ is larger than α or not. Another entanglement detection protocol employed in the main context, the purity-based protocol, states that, when

$$\text{Tr}(\rho_A^2) - \text{Tr}(\rho^2) < 0, \quad (\text{B2})$$

where ρ_A is the reduced density matrix of ρ , the state ρ is bipartite entangled.

As stated in the main context, the fidelity-based entanglement witness and the purity entanglement detection protocol can be verified using the same circuit structure as the iPPT criterion. For purity protocol, this is because

$$\text{Tr}(\rho_A^2) - \text{Tr}(\rho_{AB}^2) = \text{Tr}[(\rho \otimes \rho)(S_A \otimes \mathbb{I}_B - S_{AB})], \quad (\text{B3})$$

where the expectation value of $S_A \otimes \mathbb{I}_B - S_{AB} = S_A \otimes (\mathbb{I}_B - S_B)$ can also be estimated using BSM. Thus, by changing the reference state $|\psi\rangle$ into the same state as the target state, one can use the same circuit structure as iPPT to estimate the purity criterion. For the fidelity protocol, our conclusion is made according to the observation

$$\text{Tr}(W\rho) = \text{Tr}[(\rho \otimes \psi)(\alpha \mathbb{I} - S_{AB})], \quad (\text{B4})$$

where $\alpha \mathbb{I} - S_{AB}$ can also be estimated using BSM. However, different with iPPT and the purity protocol, the value of α need to be classically calculated according to the classical description of $|\psi\rangle$, which increases its classical computational resources consumption. Due to these reasons, we compare the iPPT protocol with these two entanglement detection protocols.

In the numerical experiments Fig. 2, we use the variational circuit shown in Fig. 5 to search for the reference state. A total of six qubits is divided into two groups, acting as subsystems A and B . A single layer of the circuit is composed of two layers of parameterized single-qubit rotation gates, $r_\theta^x = e^{i\theta X}$ and $r_\theta^z = e^{i\theta Z}$, followed by a layer of controlled-not gates. We say a circuit is of depth- k if it contains k layers. The power of iPPT protocol can be also reflected from this definition as a single layer of controlled-not gates already achieves good detection capability.

To calculate the detection probabilities, for each value of k , we sample 1000 different $2^6 \times k$ dimensional Haar random pure states. For each pure state, we trace out the k -dimensional system and leave the 2^6 dimensional mixed state. Then, we detect these 1000 mixed states using iPPT protocol with different reference state circuit depth, fidelity-based EW criterion, and the purity criterion. The probabilities are calculated using the ratio of the successfully detected states.

To compare with the fidelity-based entanglement witness protocol, we variationally search over all pure states that can be prepared via the depth-3 circuit $|\psi\rangle$, calculate the fidelity between $|\psi\rangle$ and the target state ρ , and compare it with the square of the largest Schimdt number of $|\psi\rangle$.

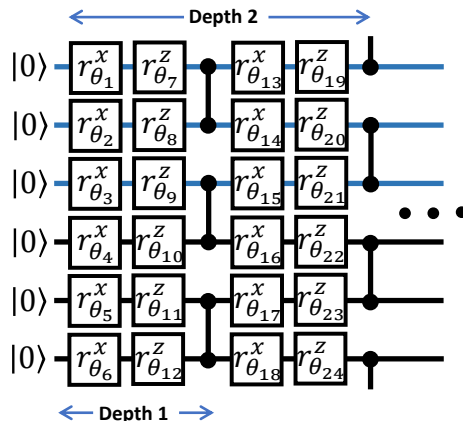


FIG. 5. Illustration of the variational circuit for preparing the reference state.

Appendix C: Fidelity-based Entanglement Witness

As introduced in Eq. (B1), entanglement in a quantum state ρ can be effectively detected with the implementation of an entanglement witness operator $W = \alpha\mathbb{I} - |\psi\rangle\langle\psi|$, where a negative expectation value, $\langle W \rangle = \text{Tr}(\rho W) < 0$, indicates the presence of entanglement. The main idea of the construction of above EW operator is measuring the distance between the prepared state and the target state $|\psi\rangle$, such as the state fidelity, to determine the entanglement property of state ρ . The construction of the above entanglement witness operator is centered around evaluating the state fidelity, i.e., measuring the proximity between the prepared state ρ and the pure entangled target state $|\psi\rangle$, so as to assess the entanglement characteristics of the state ρ . Benefiting from its relatively low measurement requirement and resource consumption, EW is effective for some simple quantum states in the experiment. Nevertheless, constructing an entanglement witness necessitates prior knowledge about the prepared state ρ , such as the specific expression of the target state $|\psi\rangle$.

In the main text, the mixed state to be measured is represented as

$$\begin{aligned} \rho_{\text{ideal}} = & 0.45(|000\rangle + |111\rangle)(\langle 000| + \langle 111|) + 0.05(|000\rangle - |111\rangle)(\langle 000| - \langle 111|) \\ & + 0.45(|100\rangle + |011\rangle)(\langle 100| + \langle 011|) + 0.05(|100\rangle - |011\rangle)(\langle 100| - \langle 011|). \end{aligned} \quad (\text{C1})$$

As indicated by its explicit expression, the closest pure entangled states to it are two GHZ-type state: $|\text{GHZ}\rangle_1 = (|000\rangle + |111\rangle)/\sqrt{2}$ and $|\text{GHZ}\rangle_2 = (|100\rangle + |011\rangle)/\sqrt{2}$. Neither of these two pure states is adequate for constructing an effective EW operator since the proportions of both are smaller than the largest Schmidt number denoted by $\alpha = 0.5$. Upon calculation, it is evident that the corresponding expectation value, $\langle W \rangle = 0.05 > 0$, indicating the inability to identify the entanglement of the quantum state. However, this does not ensure that there are no other three-qubit pure states that could potentially serve as a basis for constructing an effective EW operator to detect entanglement in the mixed state ρ_{ideal} . To eliminate the possibility of a pure state that can be used to construct an effective EW operator, we systematically examine all three-qubit pure states within the general expression of $|\phi\rangle = c_0|000\rangle + c_1|001\rangle + \dots + c_7|111\rangle$, where the coefficients c_i are complex numbers satisfying the normalization condition $\sum_{i=0}^7 |c_i|^2 = 1$. Upon systematically analyzing all three-qubit pure states numerically, we determined that the minimum EW value is $\langle W \rangle_{\text{min}} = 0.05 > 0$. This observation underscores the incapacity of the fidelity-based conventional EW to assess entanglement in the mixed state ρ_{ideal} .

Appendix D: Experimental Details of State Preparation

In our experiment, EPR photon pairs from the first two entanglement sources are “fused” into a four-photon GHZ state by interfering photons 1e and 2e on one polarizing beam splitter (PBS), PBS-1. On this basis, the reference state, $|\psi(\theta)\rangle = (|HVV\rangle + e^{i\Delta\theta}|VHV\rangle)/\sqrt{2}$, can be prepared on photons 1e-2o-2e by triggering the heralding photon 1o into the diagonal state $|+\rangle = (|H\rangle + |V\rangle)/\sqrt{2}$, rotating polarization state of photon 2o with a half-wavelength plate (HWP), and introducing relative phase $\Delta\theta$ with the wave plate combination.

As for preparation of the to-be-verified target state ρ_{exp} , the EPR pairs from the last two entanglement sources are first introduced to prepare the three-photon GHZ state, $|\text{GHZ}_3\rangle = (|HHH\rangle + |VVV\rangle)/\sqrt{2}$, by interfering photons 3e and 4e on PBS-2 and triggering the heralding photon 4o into the diagonal state $|+\rangle$. Then, polarization flipping is randomly introduced to the photon 3o with an HWP@45° driven by a linear stepping motor, transforming $|\text{GHZ}_3\rangle$ into a mixed state,

$$\begin{aligned} \rho_{\text{GHZ}} = & \frac{1}{2}(|HHH\rangle + |VVV\rangle)(\langle HHH| + \langle VVV|) \\ & + \frac{1}{2}(|VHH\rangle + |HVV\rangle)(\langle VHH| + \langle HVV|). \end{aligned} \quad (\text{D1})$$

Due to the imperfect two-photon interference on PBS-2 that mainly induces phase flip error, the to-be-verified target state in form of Eq. (4) can be actually prepared,

$$\begin{aligned} \rho_{\text{exp}} = & \frac{F_1^+}{2}(|HHH\rangle + |VVV\rangle)(\langle HHH| + \langle VVV|) + \frac{F_1^-}{2}(|HHH\rangle - |VVV\rangle)(\langle HHH| - \langle VVV|) \\ & + \frac{F_2^+}{2}(|VHH\rangle + |HVV\rangle)(\langle VHH| + \langle HVV|) + \frac{F_2^-}{2}(|VHH\rangle - |HVV\rangle)(\langle VHH| - \langle HVV|) \\ & + \frac{F'}{2}\rho'_{\text{GHZ}}. \end{aligned} \quad (\text{D2})$$

Coefficients F_i^\pm are mainly determined by the two-photon interference visibility of the PBS-2. The component state ρ'_{GHZ} represents other polarization-flipping noisy states generated during state preparation process, whose proportion F' is generally smaller than 0.05. The four GHZ states, $(|HHH\rangle \pm |VVV\rangle)/\sqrt{2}$ and $(|VHH\rangle \pm |HVV\rangle)/\sqrt{2}$, are the main component states of the target state. The component state ρ'_{GHZ} represents all other six noisy states, which are generated during the whole state preparation process. We perform the quantum state tomography measurement on the prepared target state and reconstruct its density matrix as shown in Fig. 6(b). The experimentally prepared target state is very close to the ideal case,

$$\begin{aligned} \rho_{\text{ideal}} = & 0.45(|HHH\rangle + |VVV\rangle)(\langle HHH| + \langle VVV|) + 0.05(|HHH\rangle - |VVV\rangle)(\langle HHH| - \langle VVV|) \\ & + 0.45(|VHH\rangle + |HVV\rangle)(\langle VHH| + \langle HVV|) + 0.05(|VHH\rangle - |HVV\rangle)(\langle VHH| - \langle HVV|), \end{aligned} \quad (\text{D3})$$

with the fidelity is calculated to be 0.977.

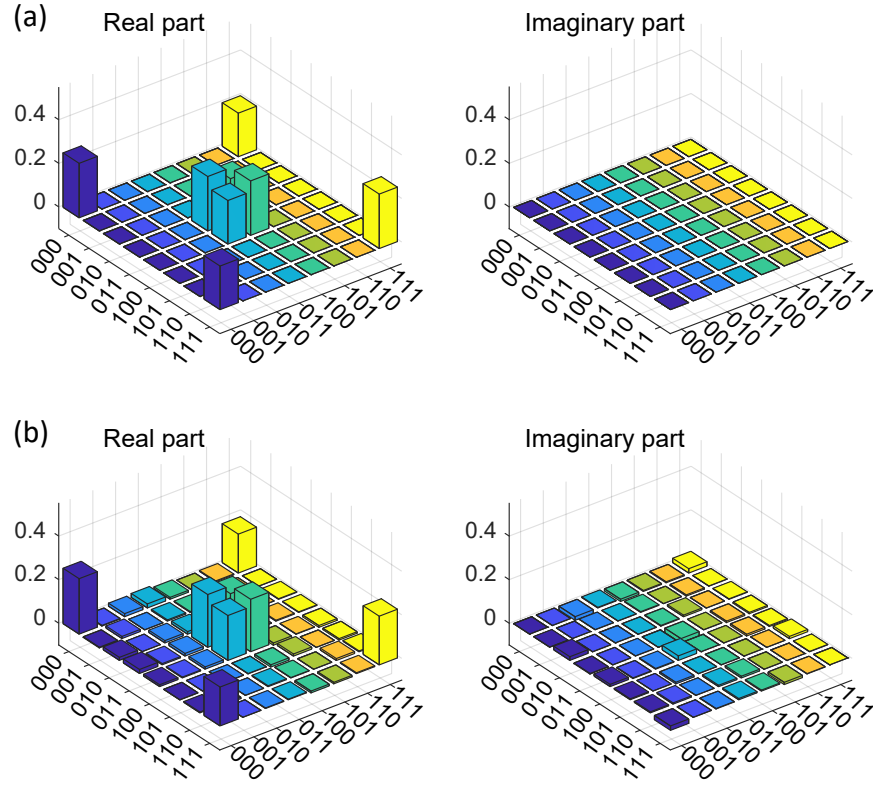


FIG. 6. (a) The density matrix of the ideal target state. (b) The density matrix of experimentally reconstructed target state.